Green Chemistry Letters and Reviews

ISSN: (Print) (Online) Journal homepage: https://www.tandfonline.com/loi/tgcl20

Ab initio chemical kinetics of Isopropyl acetate oxidation with OH radicals

Mohamed A. Abdel-Rahman, Mohamed F. Shibl, Abolfazl Shiroudi & Mohamed A. M. Mahmoud

To cite this article: Mohamed A. Abdel-Rahman, Mohamed F. Shibl, Abolfazl Shiroudi & Mohamed A. M. Mahmoud (2023) *Ab initio* chemical kinetics of Isopropyl acetate oxidation with OH radicals, Green Chemistry Letters and Reviews, 16:1, 2233539, DOI: 10.1080/17518253.2023.2233539

To link to this article: https://doi.org/10.1080/17518253.2023.2233539

GREEN CHEMISTRY LETTERS AND REVIEWS
2023, VOL. 16, NO. 1, 2233539
https://doi.org/10.1080/17518253.2023.2233539

Taylor & Francis
Taylor & Francis Group

Ab initio chemical kinetics of Isopropyl acetate oxidation with OH radicals

Mohamed A. Abdel-Rahman[a], Mohamed F. Shibl[b], Abolfazl Shiroudi[c] and Mohamed A. M. Mahmoud[d]

[a]Chemistry Department, Faculty of Science, Suez University, Suez, Egypt; [b]Center for Sustainable Development, College of Arts and Sciences, Qatar University, Doha, Qatar; [c]Department of Physical Chemistry, Gdańsk University of Technology, Gdańsk, Poland; [d]Basic Sciences Department, Tanta Higher Institute of Engineering and Technology, Tanta, Egypt

ABSTRACT

Global reactivity descriptors of isopropyl acetate (IPA) and thermo-kinetic aspects of its oxidation via OH radicals have been studied. Transition state theory (TST) was utilized to estimate the bimolecular rate constants. Ten oxidation pathways have been investigated, and all of them are exothermic. The potential energy diagram has been sketched using different pre- and post-reactive complexes for all reaction pathways. Rate coefficient calculations were obtained directly by connecting the separated reactants with different transition states. The results indicate that the reaction of IPA with OH radicals occurs in the ground state rather than the excited state, and the rate constants obtained directly and from the effective approach are the same, which confirmed the accuracy of the estimated pre-reactive complexes and the reaction mechanism. Rate constants and branching ratios show that hydrogen atom abstraction from the *iso* C – H (C_2 atom) bond is the most kinetically preferable route up to 1000 K, while at higher temperatures, H-atom abstraction from the out-of-plane CH_3 group (C_3 atom) became the most dominant route with high competition with that of the in-plane CH_3 group (C_4 atom).

ARTICLE HISTORY
Received 24 January 2023
Accepted 2 July 2023

KEYWORDS
Isopropyl acetate; oxidation; thermochemistry; chemical kinetics

1. Introduction

Esters are released into the atmosphere through both human activities, such as their use as solvents in industry and in the production of perfumes and flavors, as well as through natural sources such as vegetation, which, in addition to terpene, aldehyde, and organic acid emissions, may also produce esters and more precisely methyl esters (*1–3*). To understand their impact on atmospheric chemistry, it's essential to have precise information about their gas-phase reactions with other compounds found in the troposphere, like ozone, nitrate radicals, and hydroxyl radicals. Among these, the reaction with hydroxyl radicals is usually the most significant (*4,5*). It is crucial in influencing the oxidation power of the atmosphere (*6*).

Among all biodiesel models, isopropyl acetate (IPA) is known as the smallest branched ester that can be obtained by the reaction of isopropanol and acetic acid. IPA is used as an important organic solvent in producing many final products, such as oils, fats, perfumes, printing inks, varnishes, synthetic resins, and adhesive agents (*7,8*). Despite its simplicity, the combustion features of IPA as a biodiesel model, either alone or with oxidative agents (*9–13*), are still undiscovered in contrast to large biodiesels like methyl butanoate, ethyl acetate, methyl propionate, and ethyl propionate, which got a lot of experimental and theoretical attention (*14–18*). To determine the impact of IPA on the atmosphere, it's necessary to have precise data on its reactivity with hydroxyl radicals, which is critical for assessing its tropospheric lifetime. This information is particularly important for understanding the oxidation of IPA within combustion systems (*19*).

CONTACT Mohamed F. Shibl mfshibl@qu.edu.qa Center for Sustainable Development, College of Arts and Sciences, Qatar University, Doha 2713, Qatar
Supplemental data for this article can be accessed online at https://doi.org/10.1080/17518253.2023.2233539.

Several research groups, including Wallington *et al.* (*1*), Ferrari *et al.* (*19*), Atkinson (*20*), and Kerr and Stocker (*21*) have experimentally investigated the reaction between OH radicals and IPA. Atkinson (*20*), as well as Kerr and Stocker (*21*) used the relative rate (RR) technique with ethene at a temperature of (303 ± 2) K, while Ferrari *et al.* used RR with *n*-octane at a temperature of (295 ± 2) K.

Kerr and Stocker (*21*) conducted an experiment in a sealed Telon bag at room temperature ($T = 303 \pm 2$ K) and atmospheric pressure ($P = 750 \pm 10$ Torr). They determined the rate constant of the oxidation reaction of IPA by OH radicals to be $k = (3.0 \pm 0.8) \times 10^{-12}$ cm^3 molecule^{-1} s^{-1}. The lifetime of this reaction in the troposphere, based on an average hydroxyl radical concentration of 1×10^6 molecule cm^{-3} (*22*), is around five days. They also found that the reactivity of IPA towards OH$^{\bullet}$ radicals was low, which was an initial step towards investigating product formation in the atmosphere from the oxidation of IPA.

Wallington *et al.* (*1*) also used the flash photolysis resonance fluorescence (FP-RF) apparatus to investigate the temperature dependence of the gas-phase reactions of OH radicals with several aliphatic esters, including IPA at $T = 296$ K and over total pressure ranges of 25 – 50 Torr with argon as a diluent gas. The kinetic rate constant was determined to be $(3.72 \pm 0.29) \times 10^{-12}$ cm^3 molecule^{-1} s^{-1}. The data exhibited a negative temperature dependence at temperatures below ambient, while a positive temperature dependence was observed at higher temperatures. Furthermore, Ferrari *et al.* (*19*) found that the rate constant for the reaction between IPA and OH$^{\bullet}$ was determined in purified air at a $P = 750$ Torr and temperature of (295 ± 2) K. The rate constants for this reaction were calculated as $(3.12 \pm 0.29) \times 10^{-12}$ cm^3 molecule^{-1} s^{-1}.

In addition, Le Calvé *et al.* (*23*) used a pulsed laser photolysis-laser-induced fluorescence (PLP-LIF) apparatus to study the reaction's temperature dependence between 253 and 372 K with helium carrier gas. A least-squares fit of the experimental rate constants resulted in the following Arrhenius expression:

$$k = (0.30 \pm 60.03) \times 10^{-12} \exp[(770 \pm 52)/T] \text{cm}^3\text{molecule}^{-1}\text{s}^{-1}$$

The Arrhenius plots revealed a slightly negative temperature dependence of the rate constant for isopropyl acetate, which falls within the range of −500 K to −800 K for the studied temperature range ($T = 253 - 372$ K). This temperature dependence may suggest that weakly bound complexes are formed between IPA and OH radicals, which can either decompose back to the reactants or eliminate a water molecule. However, it's important to note that direct bimolecular reactions can also exhibit a negative temperature dependence if they have a near-zero activation energy and a pre-exponential factor that decreases with temperature (*23*). The comparison of these rate constants with those of Wallington *et al.* showed excellent agreement, while the obtained results by Kerr and Stocker were consistent within the given uncertainty ranges, despite the latter being around 20% lower (*24*).

Le Calvé *et al.* (*24*) demonstrated that the negative temperature dependence of the Arrhenius plot, which is obtained by plotting the logarithm of the rate constant, *k*, versus the inverse temperature (1/*T*), can be accurately modeled by a straight line in the studied temperature ranges. However, the slight curvature observed in the plot might indicate that *k* exhibits positive temperature dependence at higher temperatures. They proposed two possible mechanisms to explain this phenomenon: the formation of a long-lived adduct with subsequent water elimination at low temperatures and direct hydrogen transfer at high temperatures. These mechanisms could also apply to the reaction between OH radicals and isopropyl acetate. Finally, Picquet *et al.* (*25*) measured the experimental bimolecular rate coefficient at $T = 298$ K and $P = 1$ atm in a Teflon-film bag smog chamber. The bimolecular rate coefficients of oxidation of isopropyl acetate initiated by OH radicals were found to be (3.97 ± 0.18) × 10^{-12} cm^{3}molecules^{-1} s^{-1}.

An Arrhenius plot of all the kinetic rate constants that were measured or experimentally inferred over the temperature range 253–373 K is depicted in Figure 1. As is immediately apparent from this figure, for all reported series of data, the rate constant of the reactions between OH$^{\bullet}$ radicals and IPA exhibits negative temperature dependences over the studied temperature range.

The computational pyrolysis of IPA was studied previously by Silva (*9*) and via our group (*7*,*13*). Silva (*9*) performed his study at 578 – 800 K using DFT/B3LYP and *ab initio*/MP2 levels to discuss the formation of acetic acid and propene via the most stable six-membered ring transition state. El–Gogary *et al.* (*13*) discussed the thermo-kinetic aspects of IPA and isopropyl propionate using main complex fission reactions using BMK and CBS-QB3 levels at temperatures of 200 – 3000 K, while in our recent study (*26*), a full investigation was performed on the pyrolysis of IPA to show the effects of pressure and temperature variation on different possible reactions using M06-2x, ωB97XD, and CBS-QB3 levels of theory over the temperature range of 600 – 1700K and pressures ranging from 0.001–100 atm.

Hydroxyl radical is known as one of the main permanent reactive species in environmental and combustion regimes. For instance, hydroxyl radicals are the key oxidant in the global atmosphere as it controls the

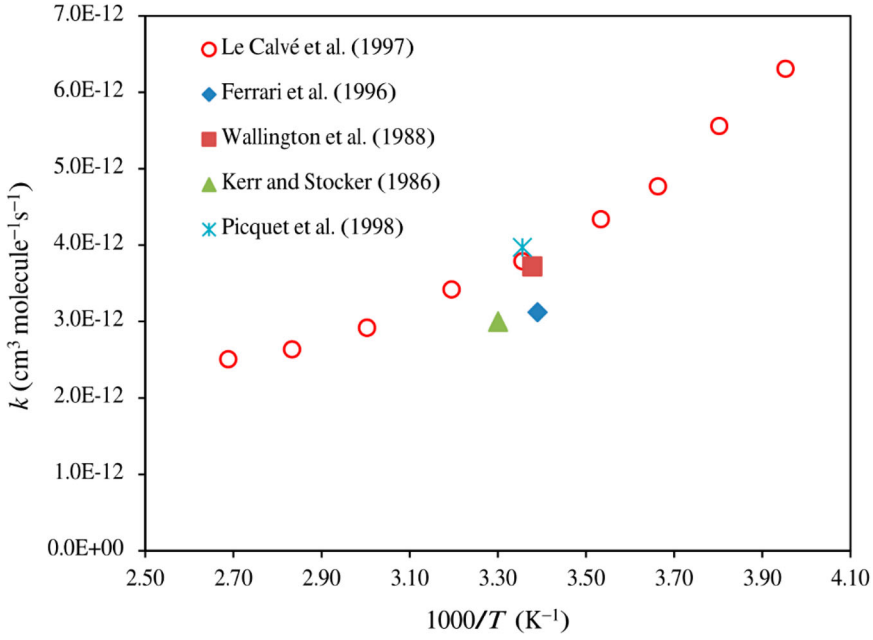

Figure 1. Arrhenius plot of the rate constants for the reactions between IPA and OH radicals.

concentrations of toxic gases (*27*) like carbon monoxide, aniline, and methane. The OH radicals has two common electronic states, the ground state ($X^2\Pi$) and the first excited state ($A^2\sum^+$). The ground state ($X^2\Pi$) is the most stable and has electron configuration $(1s)^2(2s\sigma)^2(2p\sigma)^2(2p\pi)^3$, while the $A^2\sum^+$ has electron configuration $(1s)^2(2s\sigma)^2(2p\sigma)^1(2p\pi)^4$. The ground state is more energetically preferable than the first excited state by ~ 4 eV (*28*).

Up to date, there has been neither an experimental nor a computational study on the oxidation of IPA by hydroxyl radicals under combustion conditions. Thus, this study aims to perform a computational investigation on the full oxidation mechanism of the reaction between IPA and $OH^{\bullet}$ over temperatures ranging from 253 to 373 K.

2. Computational details

2.1. Potential energy surface (PES) calculations

Structural optimization and frequency calculations for IPA, pre-reactive complexes (pre-RCs), transition states (TSs), post-reactive complexes (post-RC), and open-shell radicals were carried out at the accurate computational hybrid meta-generalized gradient Minnesota DFT/M06-2x functional (*29*) in conjunction with the correlation consistent polarized valence triplet zeta (cc-pVTZ) basis set. The vibrational frequencies were scaled by a factor of 0.9551 (*30*). The nature of the TSs is confirmed at M06-2x through the minimum energy path (MEP) (*31*) using intrinsic reaction coordinate (IRC) calculations (*32,33*). The IRC computations use 15 points both in the forward direction and the reverse direction, with a step size of 0.1 $amu^{1/2}$ Bohr. Time-dependent density functional theory (TD-DFT) calculations have been performed with the cc-pVTZ basis set to describe the reaction of IPA with the excited OH radicals. When the DFT/M06-2x method was used to estimate the electronic structures of open-shell systems, the $< S^2 >$ eigenvalues indicated spin contamination. For more accurate energies and chemical kinetic modeling, single point energy calculations for M06-2x geometries were conducted at the restricted open-shell wave functions using the *ab initio* composite methods ROCBS-QB3 (*34*) and ROCCSD(T)/cc-pVTZ (*35*) to reduce the spin contamination of the M06-2x functional (detailed structures are given in Table S1 in the Supplementary Information (SI) file). Using UCA-FUKUI software (*36*), the global reactivity descriptors of IPA such as electronic potential (μ), chemical hardness (η) (*37*), electrophilicity index (ω), softness (S) (*38*), philicities, and condensed Fukui functions have been calculated at DFT/M06-2x/cc-pVTZ level.

From previous studies (*39*), the Fukui function, $f(r)$, can reflect the reactivity of a site as given in Eq. (1):

$$f(r) = [\partial\rho(r)/\partial N]_v \quad (1)$$

where $\rho(r)$ is the electron density at r, N is the number of electrons, and $V(r)$ is the external potential (electron–nucleus attraction potential in addition to any other

potential applied to the system). The condensed Fukui function at the atom k is

$$f_k^{\infty} = \sum_{v \in k}\left[|C_{v\infty}|^2 + \sum_{\chi \notin \mu} C^*_{\chi\infty} C_{v\infty} S_{\chi v}\right] \quad (2)$$

where $C_{v\infty}$ and $S_{\chi v}$ are the molecular frontier orbital coefficients and the atomic orbital overlap matrix elements, respectively.

These definitions of the condensed Fukui function [Eqs. (2 – 5)] have been used in a variety of studies, yielding reliable results (38,40–43). The subscripts 'H' and 'L' are references to the high-occupied molecular orbital (HOMO) and low-unoccupied molecular orbital (LUMO).

$$f_k^{+} = \sum_{v \in k}\left[|C_{vL}|^2 + \sum_{\chi \notin v} C^*_{\chi L} C_{vL} S_{\chi v}\right] \text{(nucleophilic attack)} \quad (3)$$

$$f_k^{-} = \sum_{v \in k}\left[|C_{vH}|^2 + \sum_{\chi \notin v} C^*_{\chi H} C_{vH} S_{\chi v}\right] \text{(electrophilic attack)} \quad (4)$$

For a radical attack, the Fukui function can be obtained as the mean value of the Fukui functions for the nucleophilic and electrophilic attacks:

$$f_k^{o} = \frac{1}{2}(f_k^{+} + f_k^{-}) \text{(radical attack)} \quad (5)$$

using the definition of electrophilicity (44), the local electrophilicity (nucleophilic attack) Eq. (6) and the local nucleophilicity (electrophilic attack) Eq. (7) can be given by:

$$w_k^{+} = w f_k^{+} \quad (6)$$

$$w_k^{-} = w f_k^{-} \quad (7)$$

Local hardness is defined as $\eta_k = \varepsilon_L f_k^{+} - \varepsilon_H f_k^{-}$, while local softness is given by $s_k^{+} = f_k^{+} S$ and $s_k^{-} = f_k^{-} S$. For checking the multi-reference character of the calculated wave functions of different species, T_1 diagnostic calculations of the ROCBS-QB3 method were also used for TSs and the formed radicals at the ROCCSD(T)/6-31 + G(d) level for all geometries. Jensen (45) stated that when T_1 values > 0.02 that means a multi-reference nature of the used wave function, while Glowacki *et al.* (46) indicated a good harmony between ROCCSD(T) and CASPT2 results with $T_1 < 0.044$ for benzene oxidation. All calculations were carried out using the Gaussian 16 package (47), while the visualization of different molecular geometries and harmonic vibrational modes was performed using the ChemCraft package (48).

2.2. Chemical kinetic calculations

In line with energy barriers, the studied pathways exhibit global rate constants that appear to be in excellent agreement with the available experimental data, an observation that validates the two-step reaction scheme proposed by Singleton and Cvetanovic (49). To study the kinetic rate constant, the Kinetic and Statistical Thermodynamical Package (KiSThelP) (50) was used to calculate the rate coefficients of unimolecular (k_{uni}, in s^{-1}) and bimolecular (k_b, in cm^3 $molecule^{-1}s^{-1}$) reactions from the transition state theory (TST) (51). Eckart (52) tunneling correction has been used for rate constant correction:

$$\kappa_{\text{Eckart}}(T) = \frac{\exp(H_f^{\neq,0K}/k_B T)}{k_B T}\int_o^{\infty} p(E)\exp(-E/k_B T)\,dE \quad (8)$$

where k_B denotes the Boltzmann constant, h is the Plank constant, $\Delta H_f^{\neq,0K}$ represents the zero-point corrected activation enthalpy in the forward direction, and $p(E)$ is the transmission probability through the corresponding 1D barrier at energy E. The total partition function for a molecule in its ground state can be calculated from (50):

$$Q_{\text{total}} = Q_{\text{rot}} \times Q_{\text{vib}} \times Q_{\text{electr}} \times Q_{\text{trans}} \quad (9)$$

where Q_{rot}, Q_{vib}, Q_{electr}, and Q_{trans} are the rotational, vibrational, electronic, and translational partition functions. The rotational and vibrational partition functions can be calculated from the second derivatives of the energy in terms of the nuclear coordinates. The translational partition function depends on the molecular mass, pressure, and temperature of the gas, while the electronic partition function Q_{electr} can be extracted from:

$$Q_{\text{electr}} = \sum g_e \exp(-E_a/k_B T) \quad (10)$$

where g_e is the degeneracy and E_e is the electronic energy of the molecule (the difference between the energies of the ground state and exited state in the molecule).

The oxidation mechanism of the IPA reaction with OH radicals proceeds via a two-step reaction mechanism (53,54). First, the OH radical approaches the IPA molecule, and some activated pre-reactive (van der Waals) complexes are formed because of the columbic attraction between separated reactants. These complexes are more energetic and stable than the separated reactants. The activated pre-reactive complex (pre-RC) undergoes unimolecular conversion via different transition states to produce a post-reactive complex (post-RC) that ends with two separated products, P and H_2O.

These reactions can be formulated as follows:

$$\text{Step 1:IPA} + \text{OH}^{\bullet} \underset{k_{-1}}{\overset{k_1}{\rightleftharpoons}} [\text{IPA}\ldots\text{OH}]^{\bullet}$$

$$\text{Step 2:}[\text{IPA}\ldots\text{OH}]^{\bullet} \xrightarrow{k_2} \text{P} + \text{H}_2\text{O}$$

where $k_{[\text{IPA}+\text{OH}\rightarrow\text{pre-RC}]}$ is the forward rate constant for the first step (in $cm^3molecule^{-1}s^{-1}$), while k_2 and k_{-1} are the forward and reverse unimolecular reaction rate constants (in s^{-1}).

A steady-state analysis of the hydrogen abstraction process yields the effective kinetic rate constant (k_{eff}) as (*49*,*55*)

$$k_{\text{eff}} = \frac{k_1 \times k_2}{k_{-1} + k_2} \tag{11}$$

Despite the fact that the energy barrier for k_{-1} is around the same height as that for k_2, the entropy change for the reverse reaction (pre-RC→IPA + OH) is considerably greater than that for formation of the product (pre-RC→P) which can be attributed to the high values k_{-1} over k_2. This agrees with the previous results of removal of H atom from many aromatic compounds (*27*,*53*,*56*,*57*).

The total rate constant may be rewritten as.

$$k_{\text{eff}} = K_c.k_2 \tag{12}$$

with $K_c = k_1/k_{-1}$ the equilibrium constant for fast pre-equilibrium between the reactants and the pre-reactive complex, the effective rate coefficient for the studied reactions are given by (*49*)

$$k_{\text{eff}} = K_p(RT)\,k_2 \tag{13}$$

where K_c is the equilibrium constant involving concentrations and K_p is the partial pressure equilibrium constant, where $K_p = K_c\ (RT)^{\Delta n}$ and Δn is the difference between the number of moles of gaseous products and reactants and equals 0 and −1 for unimolecular and bimolecular reactions, respectively.

The equilibrium constant involving concentrations (K_c) is given by (*50*)

$$K_c = \frac{Q_{\text{PRC}}}{Q_{\text{IPA}}.Q_{\text{OH}}} \exp\left(-\frac{E_{\text{PRC}} - E_{\text{IPA}} - E_{\text{OH}}}{RT}\right) \tag{14}$$

To give a more quantitative insight into the evolution of the regioselectivity for the considered effective rate coefficients, which are obtained utilizing TST at a pressure of 1 bar and temperatures ranging from 253 to 373 K, the following is given:

$$R(i) = k_{\text{eff}}(i) / \sum_{i=1}^{n} k_{\text{eff}}(i) \tag{15}$$

3. Results and discussion

3.1. Energetic and thermodynamic parameters

As a result of $C_2 - O$ bond rotation, the **IPA** molecule has four stable conformers: **C1**, **C2**, **C**3, and **C4**. Investigation of these structures at the ROCCSD(T)/cc-pVTZ, and ROCBS-QB3//M06-2x/cc-pVTZ levels shows that the **C1** conformer is the most stable structure, while the **C2**, **C3**, and **C4** conformers have higher energies 11.33 (10.26), 53.58 (52.85) and 31.87 (32.41) kJ mol^{-1}, respectively, at the ROCBS-QB3 and ROCCSD(T) (in parentheses) levels relative to the **C1** conformer. Therefore, this study will be based on the most stable **C1** conformer unless otherwise mentioned. The optimized structures of IPA conformers and their relative energies are collected in Figures 2 and 3, respectively.

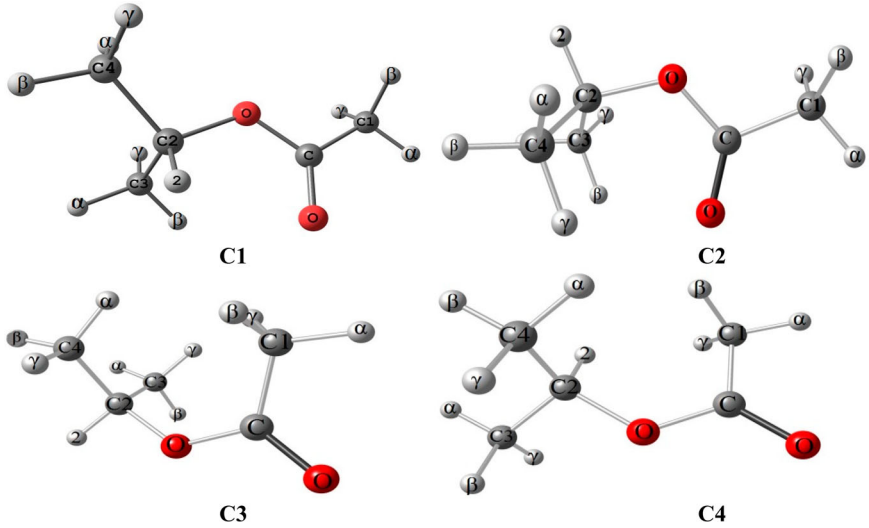

Figure 2. Optimized structures of IPA conformers C1, C2, C3, and C4.

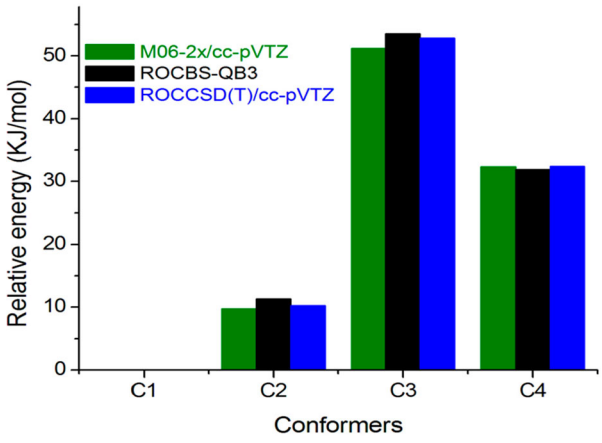

Figure 3. Relative energies of **IPA** conformers (in kJ mol^{-1}, energies calculated relative to the most stable conformer **C1**) at the M06-2x/cc-pVTZ, ROCBS-QB3, and ROCCSD(T)/cc-pVTZ levels of theory.

The energetic and thermodynamic parameters at the M06-2x/cc-pVTZ level of theory were compared to single-point energy calculations using the ROCBS-QB3 method (see Table 1). The energy differences between the M06-2x approach and the ROCBS-QB3 results are up to 0.93 kcal mol^{-1} and appear to be in good agreement (see also Table S2 of the supporting information).

According to the molecular structure of IPA (see Fig. S1) and Scheme 1, it is expected that its bimolecular oxidation mechanism by OH$^{\bullet}$ will proceed via ten different elementary hydrogen atom abstraction reactions. Fig. S1 depicts different optimized structures of pre-reactive complexes (pre-RC), transition states (TS), post-reactive complexes (post-RC), and products (P), along with the oxidation reaction of IPA by OH$^{\bullet}$ radicals, while Table S2 summarizes different thermodynamic parameters ΔE_{298K}, ΔH_{298K}, ΔS_{298K}, ΔG_{298K}, and expectation values $<S^2>$ before spin annihilation of IPA oxidation by OH$^{\bullet}$ calculated at the M06-2x/cc-pVTZ and ROCBS-QB3 levels. The potential energy profile using the M06-2x energies is shown in Figure 4. Investigation of the reaction path indicates that when OH radicals attack the IPA molecule, six different pre-reactive complexes can be formed: pre-RC$_{\{1\alpha,1\gamma\}}$, pre-RC$_{1\beta}$, pre-RC$_{\{2,3\alpha,3\beta\}}$, pre-RC$_{3\gamma}$, pre-RC$_{\{4\alpha,4\beta\}}$, and pre-RC$_{4\gamma}$. The pre-RC$_{\{1\alpha,1\gamma\}}$ occurs when H_α or H_γ is abstracted from the C_1 atom, while the pre-RC$_{\{2,3\alpha,3\beta\}}$ takes place when H_2 is abstracted from the C_2 atom, or when H_α or H_β abstracted from the C_3 atom.

Similarly, pre-RC$_{\{4\alpha,4\beta\}}$ occurs when H_α or H_β abstracted from the C_4 atom, pre-RC$_{1\beta}$ proceeds H_β of the C_1 atom, and pre-RC$_{4\gamma}$ proceeds H_γ of the C_4 atom.

Table 1. Reaction and activation parameters (in kJ mol^{-1}) for the studied pathways at the M06-2x/cc-Pvtz, and ROCBS-QB3 levels of theory. (P = 1 bar, T = 298 K).

	M06-2x/cc-pVTZ			ROCBS-QB3		
Species	ΔE_{0K}	$\Delta H°_{298K}$	$\Delta G°_{298K}$	ΔE_{0K}	$\Delta H°_{298K}$	$\Delta G°_{298K}$
IPA + OH	0.00	0.00	0.00	0.00	0.00	0.00
pre-RC$_{\{1\alpha,\ 1\gamma\}}$	−26.23	−28.71	3.51	−19.12	−21.60	10.63
pre-RC$_{1\beta}$	−19.04	−21.53	9.16	−13.24	−15.72	14.97
pre-RC$_{\{2,\ 3\alpha,\ 3\beta\}}$	−29.63	−32.11	1.84	−15.93	−18.41	15.54
pre-RC$_{3\gamma}$	−4.96	−7.45	18.00	2.16	−0.32	25.13
pre-RC$_{\{4\alpha,\ 4\beta\}}$	−4.99	−7.47	18.70	2.72	0.24	26.41
pre-RC$_{4\gamma}$	−19.46	−21.94	5.48	−14.99	−17.47	9.96
TS$_{\{1\alpha,1\gamma\}}$	4.02	1.54	39.69	7.75	5.27	43.41
TS$_{1\beta}$	6.17	3.69	43.00	9.04	6.56	45.88
TS$_2$	−15.12	−17.60	20.48	−13.53	−16.01	22.07
TS$_{3\alpha}$	6.51	4.03	38.22	9.39	6.91	41.10
TS$_{3\beta}$	−4.11	−6.60	30.13	−1.17	−3.65	33.08
TS$_{3\gamma}$	7.57	5.09	39.67	11.00	8.52	43.10
TS$_{4\alpha}$	8.20	5.72	39.13	12.13	9.65	43.06
TS$_{4\beta}$	9.17	6.69	41.10	12.63	10.15	44.56
TS$_{4\gamma}$	−4.52	−7.01	31.13	−1.56	−4.04	34.10
post-RC$_{1\alpha}$	−104.61	−107.09	−73.01	−103.32	−105.80	−71.71
post-RC$_{1\beta}$	−97.00	−99.48	−70.70	−96.20	−98.68	−69.90
post-RC$_{1\gamma}$	−104.26	−106.75	−74.76	−102.72	−105.20	−73.22
post-RC$_2$	−103.29	−105.77	−76.35	−95.27	−97.75	−68.33
post-RC$_{3\alpha}$	−72.50	−74.98	−49.41	−67.35	−69.83	−44.26
post-RC$_{3\beta}$	−89.15	−91.63	−63.95	−85.42	−87.90	−60.22
post-RC$_{3\gamma}$	−82.86	−85.34	−54.40	−74.65	−77.13	−46.19
post-RC$_{4\alpha}$	−79.85	−82.33	−51.05	−73.23	−75.71	−44.44
post-RC$_{4\beta}$	−71.90	−74.38	−49.09	−67.86	−70.34	−45.05
post-RC$_{4\gamma}$	−78.90	−81.38	−52.87	−71.41	−73.89	−45.37
P1 + H_2O	−79.19	−79.19	−81.44	−83.26	−83.26	−85.51
P2 + H_2O	−79.28	−79.28	−91.37	−80.20	−80.20	−92.29
P3 + H_2O	−61.38	−61.38	−67.37	−64.92	−64.92	−70.91
$P_{\{4\alpha,4\beta\}}$+H_2O	−60.24	−60.25	−65.66	−63.99	−63.99	−69.40
$P_{4\gamma}$ +H_2O	−59.55	−59.55	−65.49	−63.15	−63.15	−69.09

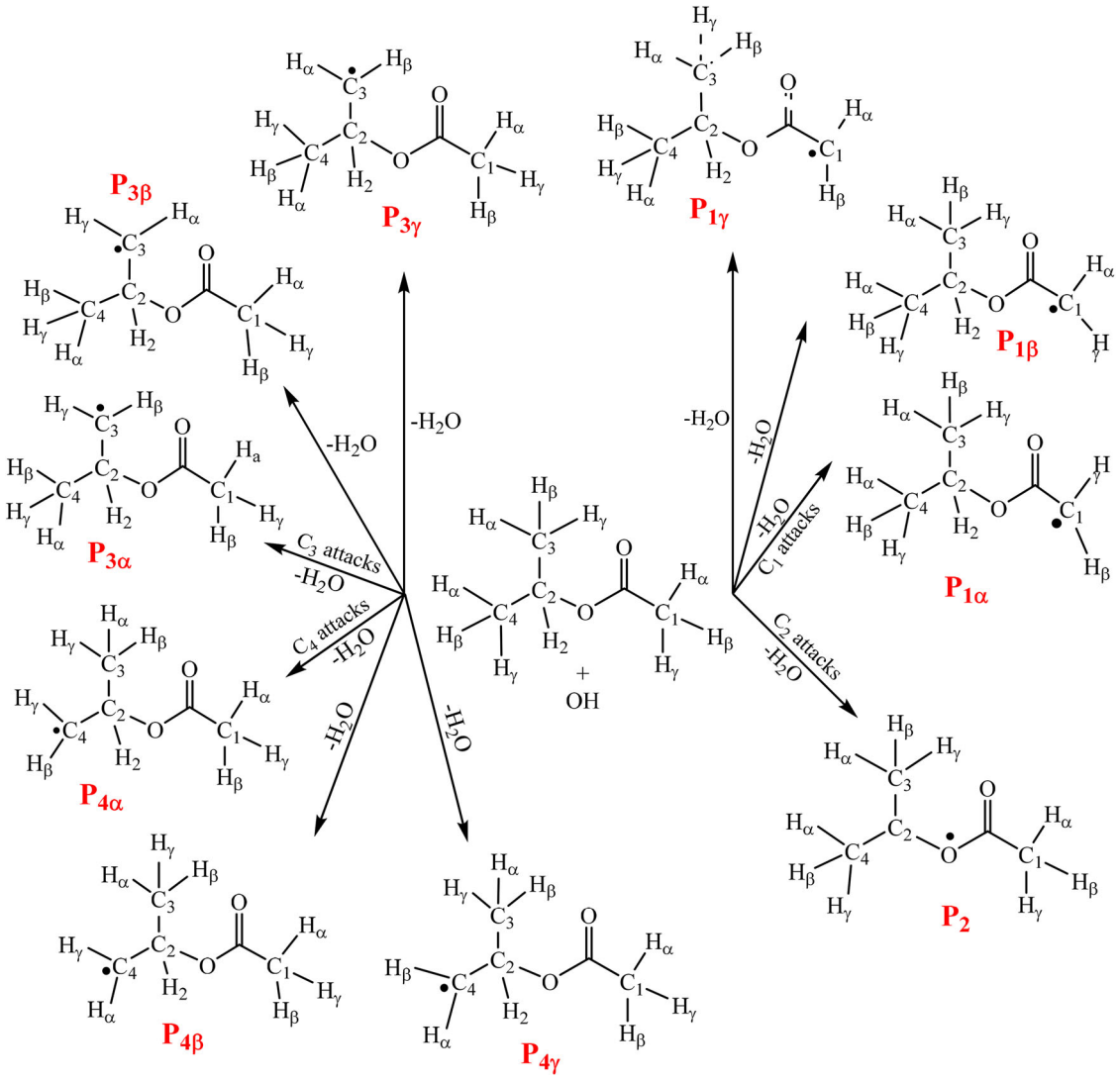

Scheme 1. Possible reaction pathways of H-atom abstraction from IPA.

These complexes are more stable than separated reactants by −19.12 (−26.23), −13.24 (−19.04), −15.93 (−29.63), 2.16 (−4.96), 2.72 (−4.99), −14.99 (−19.46) kJ mol^{-1} at the ROCBS-QB3 and M06-2x (in parentheses) methods for pre-RC$_{\{1\alpha,1\gamma\}}$, pre-RC$_{1\beta}$, pre-RC$_{\{2,3\alpha,3\beta\}}$, pre-RC$_{3\gamma}$, pre-RC$_{\{4\alpha,4\beta\}}$, and pre-RC$_{4\gamma}$, respectively. The pre-RC$_{\{1\alpha,1\gamma\}}$ is the most stable complex following the pre-RC$_{\{2,3\alpha,3\beta\}}$ by 3.2 and 3.4 kJ mol^{-1} at the ROCBS-QB3 and M06-2x methods, respectively. The stability of these pre-RCs can be attributed to the long-range Coulomb interactions between the two separated reactants (*58*).

For transition state estimation, the calculated barrier heights can be affected by the spin–orbit coupling of the OH radicals (*59,60*). However, the spin–orbit coupling of hydroxyl radicals can be depressed near the transition state, which reduces the effect on structural and vibrational frequencies. For the hydroxyl radical, the spin–orbit coupling correction is 0.84 kJ mol^{-1} (*61*), which means all calculated energies were reduced by 0.84 kJ mol^{-1}.

Li *et al.* (*62*) have previously presented theoretical calculations on the hydrogen abstraction reactions of MA by OH, CH_3, and HO_2. They used sophisticated direct dynamics computations to undertake comprehensive research on the kinetics of these H-abstraction processes. They evaluated various DFT methods to select a suitable and efficient electronic structure calculation approach for the reactions between MA and H/OH/CH_3/HO_2; furthermore, Li *et al.* investigated the impacts of different factors, such as variational effect, multistructural torsional anharmonicity, and multidimensional tunneling approximation, on rate constant determinations. They also considered the influence of OH$^{\bullet}$ spin–orbit splitting on the reactant electronic partition function for the reaction between MA and

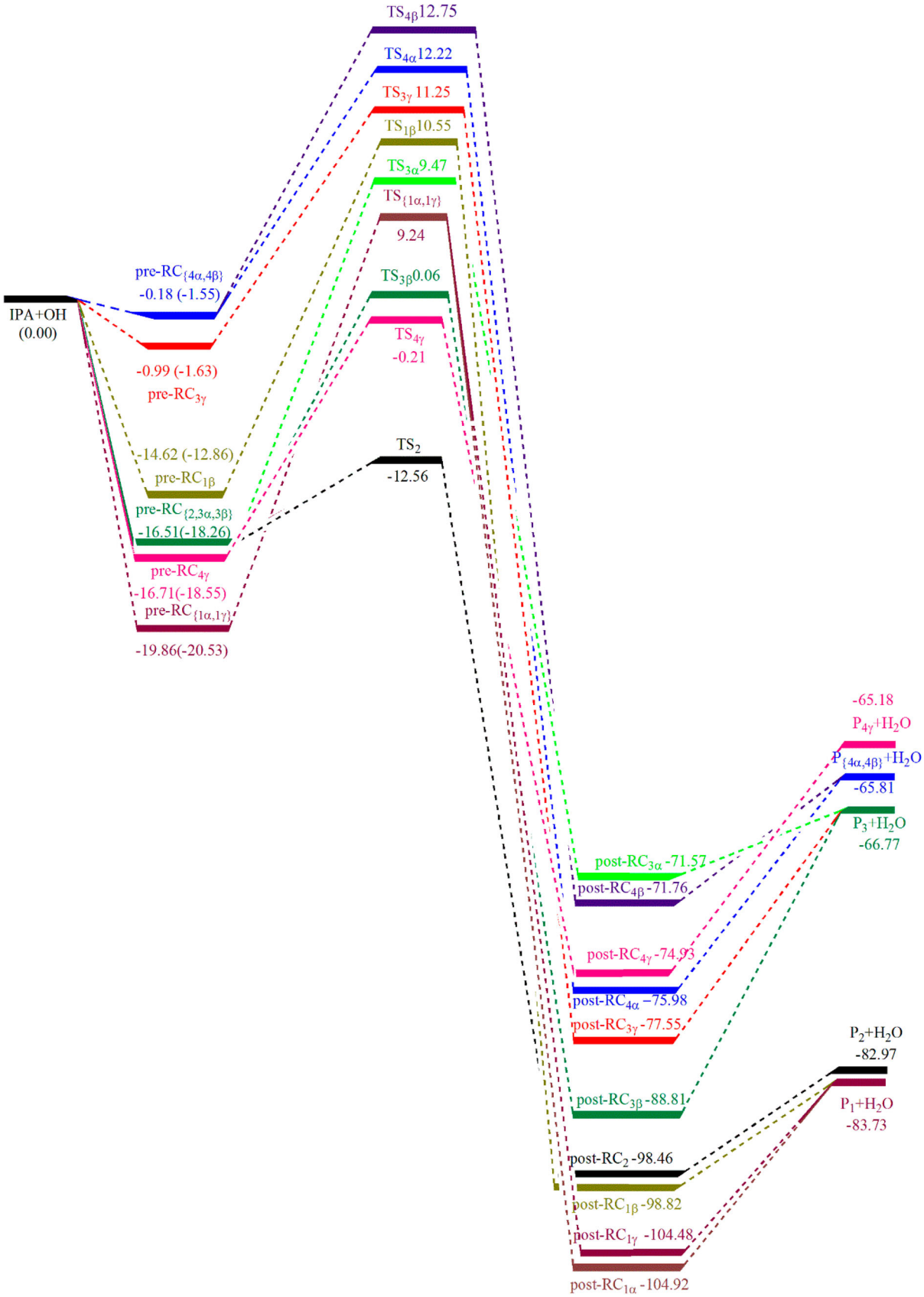

Figure 4. Energy profile (ΔE_{0K}, kJ mol^{-1}) for the reactions between IPA and OH$^{\bullet}$ at the ROCBS-QB3 and ROCCSD(T)/cc-pVTZ (in parentheses) methods.

$OH^{\bullet}$. Because the hydroxyl radical has two distinct spin–orbit components, resulting in the observation of two distinct sub-bands in $^2\sum \rightarrow {}^2\Pi$ transitions (62), this must be taken into account when studying the oxidation of MA by $OH^{\bullet}$. While estimating the OH radicals in their reactions involving $CHF_2OCF_2CHF_2 + OH$, Lily *et al.* (63) took the splitting of the ground state into account. In their rate constant estimates for the OH + CH reaction, Li and Guo (64) also took the OH spin–orbit splitting into account. Gruber and Czako (65) examined potential energy curves for $OH + CH_4/C_2H_6$ reactions with and without spin–orbit corrections. They observed that when OH reacts with CH_4/C_2H_6, the two doublet states remain quasi-degenerate without taking spin–orbit into account. With spin–orbit correction, the ground and excited states have a minor energy difference and are below and above the doublet states, respectively. As a result, it is required to investigate the effect of spin–orbit splitting on reaction rate constants (62).

At the ROCBS-QB3 and M06-2x (in parentheses) levels, we have estimated the relative energies of all TSs energies for different routes, −13.5 (−15.1), −1.6 (−4.5), −1.2 (−4.1), 7.8 (4.0), 9.0 (6.2), 9.4 (6.5), 11.0 (7.6), 12.1 (8.2), and 12.6 (9.2) kJ mol^{-1} for H-abstraction from C_2-H_2, C_4-H_γ, C_3-H_β, C_1-H_α or C_1-H_γ, C_1-H_β, C_3-H_α, C_3-H_γ, C_4-H_α, and C_4-H_β bonds, respectively. From the past results, it is clear that H atom abstraction from C_2, H_γ of C_4, and H_β of C_4 are the most kinetically favorable routes with negative energy barriers and have comparable energies at ROCBS-QB3 and M06-2x levels. The preferable H-abstraction from these sites can be attributed to the hydrogen bond stabilization of the transition state. The obtained energies at the M06-2x level differ from those of ROCBS-QB3 by 4.5 – 13.7 kJ mol^{-1} for pre-RCs, 1.6 – 3.9 kJ mol^{-1} for TS states, 0.8 – 8.0 kJ mol^{-1} for post-RCs, and 0.9 – 4.1 kJ mol^{-1} for separated products. The high energy gap can be attributed to the high spin contamination $<S^2>$ of the DFT/M06-2x method during the oxidation reactions. Inspection of T_1 diagnostics (Table S2) reveals high relative values for TSs 0.022 – 0.029, followed by 0.016 – 0.017 for products, 0.015 – 0.016 for post-RCs, and 0.014 – 0.015 for pre-RCs.

At both the ROCBS-QB3 and M06-2x levels (see Table S2 of the SI), all reactions are exothermic ($\Delta H < 0$) and exoergic ($\Delta G < 0$). The most exothermic and spontaneous reaction channel is **P1** ($\Delta H = -83.3$ and $\Delta G = -85.5$ kJ mol^{-1}) followed by **P2** ($\Delta H = -80.2$ and $\Delta G = -92.3$ kJ mol^{-1}). The high stability of the **P1** radical can be attributed to the resonance of the π_{C-O} bond with the free electron of the CH_2 radical, while the stability of **P2** can be attributed to the interaction of the oxygen lone pairs of an electron with the adjacent free electron of the central C-atom. Inspection of ΔS^o for pre- and post-reactive complexes and transition state structures indicates negative values, which may be related to combining two moles of separated reactants to produce only one mole of a complex, while in final products ΔS^o signs are slightly positive (0.01 – 0.04 kJ mol^{-1}) which can be attributed to the existence of an unsaturated radical.

According to Hammond's postulate (66), for a chemical reaction, the endothermicity or exothermicity of the reaction can be attributed to the lateness (*L*) of the selected transition state. The transition state encounters a shorter forming bond late, and the reaction is endothermic, while the transition state contains a shorter breaking bond early, and the reaction is exothermic. The numerical value of lateness (*L*) can be calculated from Table 2:

$$L = \frac{B_{react} - B^{TS}_{react}}{B_{prod} - B^{TS}_{prod}} \quad (16)$$

B_{react} is the bond lengths of the breaking C–H bond in the IPA and B_{prod} is the forming H–O bond in H_2O. B^{TS}_{react} and B^{TS}_{prod} are the bond lengths of the C–H bond breaking and the H–O bond forming in the transition state, respectively. In the case of $L > 1$, the transition state structure is product-like and the reaction is endothermic, while in the case of L ? 1 the transition state structure is reactant-like and the reaction is exothermic. The geometrical parameters of transition state structures and the *L* parameters for the bimolecular reaction of IPA with OH radicals at the M06-2x/cc-pVTZ level are given in Table 3. The results indicate that all reactions are strongly exothermic and consistent with the data given in Figure 4.

3.2. Frontier molecular orbitals (FMO) reactivity indexes

Softness and hardness are related to the reactivity and stability of chemical molecules. Hardness shows the ability of chemicals to resist polarization. The less

Table 2. Geometrical parameters (Å) of transition state structures and L parameters for the bimolecular reaction of IPA with OH radicals at the M06-2x/cc-pVTZ level of theory.

H-atom abstraction	B_{react}	B^{TS}_{react}	B_{prod}	B^{TS}_{prod}	*L* parameter
$H_{1\alpha}$ /$H_{1\gamma}$	1.0845	1.2171	0.9589	1.2890	0.40
$H_{1\beta}$	1.0845	1.2016	0.9589	1.3244	0.32
H_2	1.0900	1.1663	0.9589	1.4021	0.17
$H_{3\alpha}$	1.0899	1.1813	0.9589	1.3727	0.22
$H_{3\beta}$	1.0879	1.1997	0.9589	1.3248	0.30
$H_{3\gamma}$	1.0906	1.1778	0.9589	1.3862	0.20
$H_{4\alpha}$	1.0903	1.1794	0.9589	1.3819	0.21
$H_{4\beta}$	1.0894	1.1846	0.9589	1.3611	0.24
$H_{4\gamma}$	1.0879	1.1994	0.9589	1.3249	0.30

Table 3. Calculated excitation energies (eV), wavelengths (nm), and oscillator strength (a.u.) of pre- and post-reactive complexes at the TDDFT-M06-2x/cc-pVTZ//M06-2x/cc-pVTZ level.

Structure	Excited state No	Excitation energy (eV)	Wavelength (nm)	Oscillator strength (a.u.)
pre-$RC_{\{1\alpha,\ 1\gamma\}}$	1	0.3155	3930.19	0.0000
	2	4.2792	289.73	0.0017
	3	6.6175	187.36	0.0000
pre-$RC_{1\beta}$	1	0.2647	4684.30	0.0000
	2	4.3708	283.66	0.0022
	3	6.2259	199.14	0.0000
pre-$RC_{\{2,\ 3\alpha,\ 3\beta\}}$	1	0.2497	4966.30	0.0000
	2	4.2815	289.58	0.0019
	3	6.5166	190.26	0.0000
pre-$RC_{3\gamma}$	1	0.3642	3403.84	0.0000
	2	6.2646	197.91	0.0000
	3	6.4213	193.08	0.0000
pre-$RC_{\{4\alpha,\ 4\beta\}}$	1	0.3544	3498.19	0.0000
	2	4.6849	264.65	0.0026
	3	6.2594	198.08	0.0000
pre-$RC_{4\gamma}$	1	0.3051	4064.28	0.0000
	2	4.3346	286.03	0.0022
	3	6.2246	199.18	0.0000
post-$RC_{1\alpha}$	1	4.4939	275.89	0.0000
	2	5.4546	227.30	0.0342
	3	7.3275	169.20	0.0000
post-$RC_{1\beta}$	1	4.1622	297.88	0.0000
	2	5.4098	229.19	0.0362
	3	7.3312	169.12	0.0000
post-$RC_{1\gamma}$	1	4.5229	274.12	0.0000
	2	5.4956	225.60	0.0337
	3	7.1112	174.35	0.0001
post-RC_2	1	6.3281	195.93	0.0000
	2	6.4527	192.14	0.0003
	3	7.0000	177.12	0.0020
post-$RC_{3\alpha}$	1	6.2845	197.29	0.0000
	2	6.4452	192.37	0.0000
	3	6.9513	178.36	0.0017
post-$RC_{3\beta}$	1	6.4658	191.75	0.0000
	2	6.5881	188.19	0.0000
	3	7.1265	173.98	0.0024
post-$RC_{3\gamma}$	1	6.4144	193.29	0.0000
	2	6.6277	187.07	0.0000
	3	7.0541	175.76	0.0024
post-$RC_{4\alpha}$	1	6.2259	199.14	0.0000
	2	6.4102	193.42	0.0000
	3	6.9114	179.39	0.0019
post-$RC_{4\beta}$	1	6.2661	197.87	0.0000
	2	6.4359	192.65	0.0000
	3	6.9434	178.56	0.0021
post-$RC_{4\gamma}$	1	6.4305	192.81	0.0000
	2	6.6185	187.33	0.0000
	3	7.0941	174.77	0.0024

polarizable molecules are the harder ones, and vice versa. Soft molecules are considered reactive, polarizable, and less stable, while hard molecules are non-polarizable, unreactive, and more stable. Tables S3 and S4 collect the global reactivity descriptors of IPA (electronic potential, softness, hardness, and electrophilicity) and local atomic descriptors (Fukui functions for the nucleophilic, electrophilic, and free radical attacks, hardness, and electrophilicity). The softness of IPA is 2.4635 a.u. which is close to that of similar ketones (*67*). This data indicates that IPA is more polarizable and reactive than ketones. In this study, the reactions of IPA with OH radicals involve free radical attacks, so the estimation of the Fukui function for the free radical attack, f^o, is important. The susceptibility to free radical attack of C_2 ($f^o = 0.1092$) is greater than that of C_1 ($f^o = 0.0878$), C_4 ($f^o = 0.0186$), and C_3 ($f^o = 0.0184$).

3.3. Excited state calculations

The oxidation reaction mechanism of IPA and the excited OH radicals was investigated using the time-dependent density functional theory TDDFT-M06-2x/cc-pVTZ//M06-2x/cc-pVTZ level. The obtained wavelengths, vertical excitation energies, and oscillator strengths of different pre- and post-reactive complexes are given in Table 3.

Based on the obtained results in Table 3, the pre-$RC_{\{2,3\alpha,3\beta\}}$, pre-$RC_{1\beta}$, pre-$RC_{4\gamma}$, pre-$RC_{\{1\alpha,1\gamma\}}$ are quite more photolyzed than the pre-$RC_{\{4\alpha,4\beta\}}$ and pre-$RC_{3\gamma}$ because of the first excited state energies. These results agree with the obtained relative energies on the potential energy diagram (Figure 4). To reach the 1st excited state, the ground pre-$RC_{\{1\alpha,1\gamma\}}$, pre-$RC_{1\beta}$, pre-$RC_{\{2,3\alpha,3\beta\}}$, pre-$RC_{3\gamma}$, pre-$RC_{\{4\alpha,4\beta\}}$ and pre-$RC_{4\gamma}$ require 30.44, 25.54, 24.09, 35.14, 34.20, and 29.44 kJ mol^{-1}, respectively.

The most dominant kinetic route **P2** and thermodynamic route **P1** (from H_α abstraction) require 610.61 and 433.62 kJ mol^{-1}, respectively, which are too large for their ground state energies, proving that the oxidation reaction of IPA by $OH^{\bullet}$ occurs in the ground state rather than the excited state.

3.4. Chemical kinetic rate constants

The bimolecular rate constants for all elementary H-abstraction pathways are estimated by using the TST in connection with the Eckart tunneling coefficient at the studied temperatures and a pressure of 1 bar, which are summarized in Table 4. In this table, theoretical rate constants can also be compared with available experimental data (*1*,*19*–*24*). Table 4 collects the effective TST rate constants for the oxidation of IPA with the OH radicals at a temperature ranging from 253 to 373 K using ROCBS-QB3 energies. Based on the obtained results, rate constants using the three different methods are comparable and exhibit a positive temperature dependency; in addition, the total rate constant increases with the increase in temperature. It is noted that the Eckart tunneling values of all hydrogen atom abstractions are large at low temperatures (Table S5). At $T = 298$ K and $P = 1$ atm, the total computational bimolecular TST rate constant using ROCBS-QB3 energies is 5.37×10^{-11} cm^3 $molecule^{-1}$ s^{-1} which is close to the available experimental data.

Table 4. Effective TST rate constants (in cm^3 $molecule^{-1}s^{-1}$ unit) for oxidation of IPA by OH radicals over temperatures 253 – 373 K at the M06-2x/cc-pVTZ level of theory.

T(K)	$k_{(TS1\alpha)}$	$k_{(TS1\beta)}$	$k_{(TS1\gamma)}$	$k_{(TS2)}$	$k_{(TS3\alpha)}$	$k_{(TS3\beta)}$	$k_{(TS3\gamma)}$	$k_{(TS4\alpha)}$	$k_{(TS4\beta)}$	$k_{(TS4\gamma)}$	$k_{exp.}$
253	9.0×10^{-13}	7.1×10^{-14}	8.9×10^{-13}	3.4×10^{-10}	1.2×10^{-13}	1.7×10^{-11}	3.7×10^{-14}	4.8×10^{-14}	2.5×10^{-14}	7.5×10^{-12}	$(6.31\pm0.30)\times10^{-12}$ (*24*)
											$(6.46\pm0.06)\times10^{-12}$ (*24*)
263	7.2×10^{-13}	6.4×10^{-14}	7.1×10^{-13}	2.6×10^{-10}	1.2×10^{-13}	1.3×10^{-11}	4.1×10^{-14}	5.3×10^{-14}	2.7×10^{-14}	6.2×10^{-12}	$(5.56\pm0.07)\times10^{-12}$ (*24*)
273	5.9×10^{-13}	6.0×10^{-14}	5.9×10^{-13}	2.0×10^{-10}	1.2×10^{-13}	1.1×10^{-11}	4.5×10^{-14}	5.9×10^{-14}	3.0×10^{-14}	5.2×10^{-12}	$(4.77\pm0.14)\times10^{-12}$ (*24*)
283	5.0×10^{-13}	5.6×10^{-14}	5.0×10^{-13}	1.5×10^{-10}	1.3×10^{-13}	8.8×10^{-12}	5.0×10^{-14}	6.5×10^{-14}	3.3×10^{-14}	4.5×10^{-12}	$(4.34\pm0.08)\times10^{-12}$ (*24*)
293	4.4×10^{-13}	5.4×10^{-14}	4.3×10^{-13}	1.2×10^{-10}	1.3×10^{-13}	7.4×10^{-12}	5.4×10^{-14}	7.2×10^{-14}	3.7×10^{-14}	3.9×10^{-12}	
298	4.1×10^{-13}	5.3×10^{-14}	4.1×10^{-13}	1.1×10^{-10}	1.4×10^{-13}	6.9×10^{-12}	5.7×10^{-14}	7.5×10^{-14}	3.9×10^{-14}	3.6×10^{-12}	$(3.12\pm0.29)\times10^{-12}$ (295 K) (*19*)
											$(3.72\pm0.29)\times10^{-12}$ (296 K) (*1*)
											$(3.77\pm0.29)\times10^{-12}$ (*24*)
											$(3.80\pm0.07)\times10^{-12}$ (*24*)
											$(3.85\pm0.10)\times10^{-12}$ (*24*)
											$(3.75\pm0.12)\times10^{-12}$ (*24*)
											$(3.96\pm0.10)\times10^{-12}$ (*25*)
											$(3.98\pm0.18)\times10^{-12}$ (*25*)
303	3.9×10^{-13}	5.2×10^{-14}	3.9×10^{-13}	1.0×10^{-10}	1.4×10^{-13}	6.4×10^{-12}	6.0×10^{-14}	7.9×10^{-14}	4.1×10^{-14}	3.4×10^{-12}	$(3.08\pm0.84)\times10^{-12}$ (*21*)
											$(3.0\pm0.8)\times10^{-12}$ (*20*)
313	3.5×10^{-13}	5.1×10^{-14}	3.5×10^{-13}	8.2×10^{-11}	1.5×10^{-13}	5.7×10^{-12}	6.5×10^{-14}	8.6×10^{-14}	4.5×10^{-14}	3.1×10^{-12}	
323	3.2×10^{-13}	5.1×10^{-14}	3.2×10^{-13}	6.9×10^{-11}	1.6×10^{-13}	5.1×10^{-12}	7.1×10^{-14}	9.4×10^{-14}	4.9×10^{-14}	2.8×10^{-12}	
333	3.0×10^{-13}	5.1×10^{-14}	3.0×10^{-13}	5.9×10^{-11}	1.6×10^{-13}	4.6×10^{-12}	7.7×10^{-14}	1.0×10^{-13}	5.4×10^{-14}	2.6×10^{-12}	$(2.92\pm0.05)\times10^{-12}$ (*24*)
343	2.8×10^{-13}	5.1×10^{-14}	2.8×10^{-13}	5.1×10^{-11}	1.7×10^{-13}	4.2×10^{-12}	8.3×10^{-14}	1.1×10^{-13}	5.9×10^{-14}	2.4×10^{-12}	
353	2.7×10^{-13}	5.1×10^{-14}	2.7×10^{-13}	4.4×10^{-11}	1.8×10^{-13}	3.9×10^{-12}	9.0×10^{-14}	1.2×10^{-13}	6.4×10^{-14}	2.2×10^{-12}	$(2.64\pm0.06)\times10^{-12}$ (*24*)
363	2.6×10^{-13}	5.2×10^{-14}	2.6×10^{-13}	3.9×10^{-11}	1.9×10^{-13}	3.6×10^{-12}	9.7×10^{-14}	1.3×10^{-13}	7.0×10^{-14}	2.1×10^{-12}	
373	2.5×10^{-13}	5.2×10^{-14}	2.5×10^{-13}	3.4×10^{-11}	2.0×10^{-13}	3.4×10^{-12}	1.0×10^{-13}	1.4×10^{-13}	7.6×10^{-14}	1.9×10^{-12}	$(2.49\pm0.08)\times10^{-12}$ (372 K) (*24*)
											$(2.53\pm0.09)\times10^{-12}$ (372 K) (*24*)

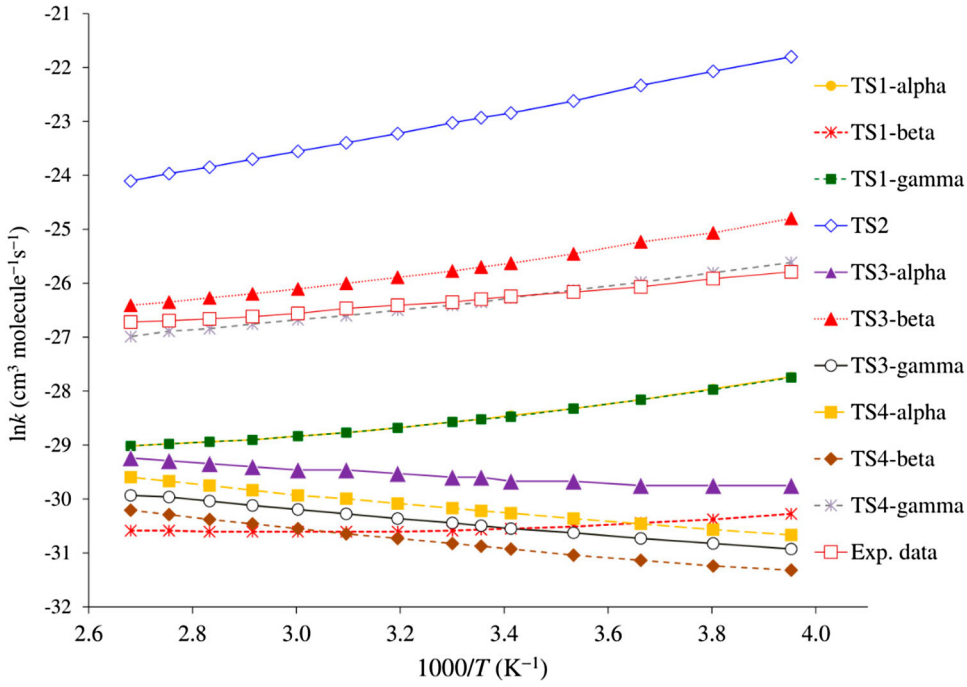

Figure 5. Arrhenius plot of the obtained TST bimolecular rate constants using the M06-2x approach ($P = 1$ bar) versus experimental data (*24*).

Based on the computed M06-2*x* energy profiles and related vibrational frequencies, the TST calculation yielded Eckart tunneling correction, $\kappa(T)$ values for the examined pathways (see Table S5 of the SI). These results reveal that the tunneling factor's effects are effective in determining the reaction rate in the studied temperature ranges. Also, the forward and reverse unimolecular rate constants (in s^{-1}) using TST for oxidation of IPA by OH radicals over the studied temperature ranges at the M06-2x/cc-pVTZ level are summarized in Table S6 of the SI. The results reveal that the backward chemical paths of the studied reactions are much faster than the forward chemical pathways. As a result, to evaluate the possibility of the examined reactions here, the subsequent reactions of the corresponding adducts in these reactions should be taken into account. TST estimations for unimolecular (k_2) and effective bimolecular (k_{eff}) rate constants were performed over temperature ranges of 253 – 373 K and a pressure of 1 bar, and the obtained effective rate coefficients were compared with the available experimental data. (see Table 4).

Figure 5 shows an Arrhenius plot of the obtained TST values for the effective rate constants of the studied pathways. The oxidation pathways involving TS3α, TS4α, and TS4β species are positively dependent on temperature, while the opposite is true for other pathways involving TS1α, TS1β, TS1γ, TS2, TS3β, TS3γ, and TS3γ species. It is worth noting that, in line with available experimental data (*1*,*19*–*24*), TST effective rate coefficients for the dominant pathway involving TS2 species are negatively dependent on temperature, which is a consequence of negative activation energies for the first bimolecular reaction steps. The TST results suggest that the effective rate constants, k_{eff}(TS2) are much larger than the effective rate constants for other reaction pathways, by factors ranging from 10 to 13600. As a result, the production of a water molecule and the P2 radical will dominate the overall reaction mechanism under atmospheric pressure and at temperatures ranging from 253 to 373 K.

Table 5 represents the contribution of different H abstractions during the oxidation of IPA by OH radicals at a pressure of 1 bar and over temperature ranges of 253 – 373 K. The results indicate the dominance of H-atom abstraction from the –CH group as the main H-abstraction reaction. The total rate constant for H-atom abstraction from the $-CH_3C(=O)-$ site (C_1 atom) can be calculated from the sum of the individual rate constants of the three H-atom abstraction pathways, H_α, H_β, and H_γ, $k_1 = k(TS_{1\alpha})+k(TS_{1\beta})+k(TS_{1\gamma})$, Similarly, for H-atom abstraction from –CH–(C_2 atom), $k_2 = k(TS_2)$, out-of-plane $-CH_3$ (C_3), $k_3 = k(TS_{3\alpha})+k(TS_{3\beta})+k(TS_{3\gamma})$, and in-plane $-CH_3$ (C_4), $k_4 = k(TS_{4\alpha})+k(TS_{4\beta})+k(TS_{4\gamma})$. The overall rate constant for the reactions between IPA and OH$^\bullet$, $k_{total} = k_1 + k_2 + k_3 + k_4$, and the branching ratio $(BR_i) = k_i / k_{total}$, where $i = 1 - 4$.

Based on the M06-2x method's calculated branching ratios, the primary hydrogen removal atom from IPA through transition states TS2, TS3β, and TS4γ is expected

Table 5. TST Branching ratios for all studied combustion reactions between IPA and OH radicals using the M06-2x method.

	Branching ratios									
T(K)	TS1α	TS1β	TS1γ	TS2	TS3α	TS3β	TS3γ	TS4α	TS4β	TS4γ
253	0.25	0.02	0.24	92.75	0.03	4.64	0.01	0.01	0.01	2.05
263	0.26	0.02	0.25	92.55	0.04	4.63	0.01	0.02	0.01	2.21
273	0.27	0.03	0.27	91.87	0.06	5.05	0.02	0.03	0.01	2.39
283	0.30	0.03	0.30	91.11	0.08	5.35	0.03	0.04	0.02	2.73
293	0.33	0.04	0.32	90.55	0.10	5.58	0.04	0.05	0.03	2.94
298	0.34	0.04	0.34	90.40	0.12	5.67	0.05	0.06	0.03	2.96
303	0.35	0.05	0.35	90.13	0.13	5.77	0.05	0.07	0.04	3.06
313	0.38	0.06	0.38	89.23	0.16	6.20	0.07	0.09	0.05	3.37
323	0.41	0.07	0.41	88.50	0.21	6.54	0.09	0.12	0.06	3.59
333	0.45	0.08	0.45	87.74	0.24	6.84	0.11	0.15	0.08	3.87
343	0.48	0.09	0.48	86.98	0.29	7.16	0.14	0.19	0.10	4.09
353	0.53	0.10	0.53	86.03	0.35	7.63	0.18	0.23	0.13	4.30
363	0.57	0.11	0.57	85.23	0.42	7.87	0.21	0.28	0.15	4.59
373	0.62	0.13	0.62	84.23	0.50	8.42	0.25	0.35	0.19	4.71

to be 84.23 – 92.75%, 4.64-8.42% and 2.05 – 4.71%, respectively. As can be seen from Figure 6 and Table 5, at the M06-2x method ($P = 1$ bar and $T = 298$ K), the branching ratio for the pathway involving TS2 species decreases gradually with increasing temperature, while the opposite is true for other pathways (involving TS3β and TS4γ species).

Conclusions

This study utilized the M06-2x method and cc-pVTZ basis set to investigate the gas phase reaction mechanism of OH-initiated isopropyl acetate (IPA) oxidation. Geometries were optimized, and frequencies were analyzed for all stationary points on the potential energy surfaces. The energies of these stationary points were then inspected using the ROCBS-QB3 method on the optimized geometries at the M06-2x/cc-pVTZ level at a pressure of 1 bar and over temperature ranges of 253 – 373 K.

Consistent with the available experimental data, because of the formation of a pre-reactive van der Waals (VdW) molecular complex [IPA … OH]$^{\bullet}$, the corresponding transition state lies below the isolated reactants, hence an effective negative activation energy of around −15.12 (−13.53) kJ mol^{-1} on the pathway leading to the $CH_3C(O)_2$-$C^{\bullet}(CH_3)_2$ radical at the M06-2x (ROCBS-QB3) method.

The energy profiles obtained from the calculations were used to determine the kinetic rate constants and branching ratios under atmospheric pressure using transition state theory. The data revealed that the hydrogen atom removal from the C_2 position of the IPA produces the most abundant product, which is attributed to the hydrogen bond stabilization of the transition state, and is under kinetic control of the reaction. These findings were consistent with the available experimental rate constants and support the validity of the two-step reaction scheme proposed by Singleton and Cvetanovic (*49*). The calculated branching ratios also suggest that the

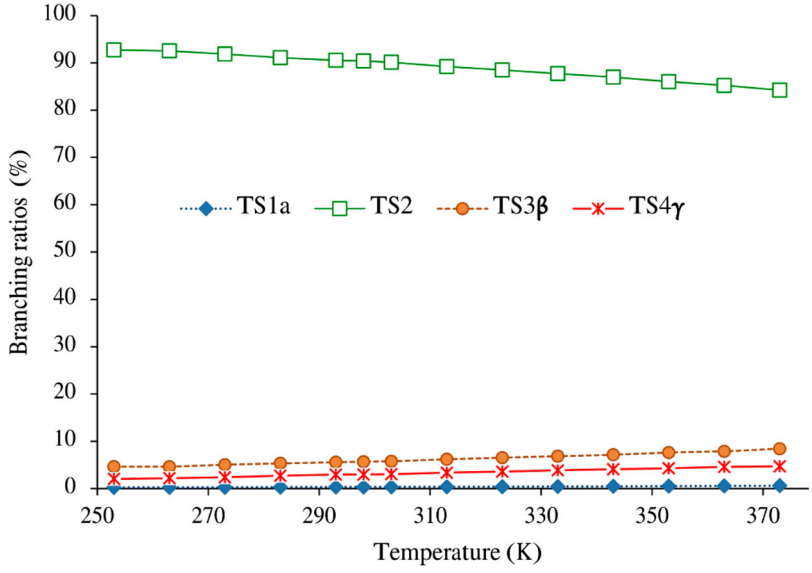

Figure 6. Branching ratios for accumulative H-abstraction along with the IPA oxidation and OH radicals.

regioselectivity of the primary reaction pathway decreases as the temperature increases. The obtained results can be summarized as follows:

[1] The order of H-abstraction reactions from IPA by the $OH^{\bullet}$, as determined from energy barrier calculations, is $TS_2 < TS_{4\gamma} < TS_{3\beta} < TS_{\{1\alpha,\ 1\gamma\}} < TS_{1\beta} < TS_{3\alpha} < TS_{3\gamma} < TS_{4\alpha} < TS_{4\beta}$.

[2] Based on condensed Fukui functions, the susceptibility to free radical attack is in the order of $C_2 > C_1 > C_4 > C_3$.

[3] All of the reactions investigated are thermodynamic in nature, with H-abstraction from the C_1 position (CH_3-C = O) and C_2 position (C – H) being the most exothermic reactions.

Acknowledgment

The authors dedicate this manuscript to the soul of Prof. Ahmed El-Nahas, without whom this project would never have been possible. The authors thank the anonymous referees for their stimulating objections and highly relevant comments. The publication of this article was funded by the Qatar National Library.

Authors' contributions

Mohamed A. Abdel-Rahman: Visualization, Data curation, Investigation, Formal analysis, Writing-original draft, Project administration.

Mohamed F. Shibl: Conceptualization, Methodology, Data curation, Formal analysis, Investigation, Writing-review & editing.

Abolfazl Shiroudi: Conceptualization, Methodology, Data curation, Formal analysis, Investigation, Writing-review & editing.

Mohamed A. M. Mahmoud: Conceptualization, Methodology, Data curation, Formal analysis, Investigation, Writing-review & editing.

Disclosure statement

No potential conflict of interest was reported by the author(s).

Funding

This work was supported by Qatar National Library.

References

[1] Wallington, T.J.; Dagaut, P.; Liu, R.; Kurylo, M.J. *Int. J. Chem. Kinet.* **1988,** *20*, 177–186.
[2] Arey, J.; Winer, A.M.; Atkinson, R.; Aschmann, S.M.; Long, W.D.; Morrison, C.L.; Olszyk, D.M. *J. Geophys. Res.* **1991,** *96*, 9329.
[3] Steinbrecher, R. In *Proceedings of EUROTRAC Symposium '94*; Borrell, P.M., et al. Eds.; SPB *Academic Publishing* bv: The Hague, The Netherlands, 1994; pp.480-484.
[4] Bunce, N.J.; Liu, L.; Zhu, J. *Environ. Sci. Technol.* **1997**, *31*, 2252–2259.
[5] Atkinson, R.; Arey, J. *Environ. Health Perspect.* **1994**, *102*, 117–126.
[6] Qu, X.; Zhang, Q.; Wang, W. *Chem. Phys. Lett.* **2006**, *429*, 77–85.
[7] Lee, H.-Y.; Lai, I.-K.; Huang, H.-P.; Chien, I.-L. *Ind. Eng. Chem. Res.* **2012,** *51* (22), 11753–11763.
[8] Zhang, B.J.; Yang, W.S.; Hu, S.; Liang, Y.Z.; Chen, Q.L. *Chem. Eng. Process.* **2013**, *70*, 117–130.
[9] Silva, A.M. *Chem. Phys. Lett.* **2007**, *439* (1-3), 8–13.
[10] de Sarmiento, M.A.G.; Domınguez, R.M.; Chuchani, G. *J. Phys. Chem. A* **1980,** *84* (16), 2531–2535.
[11] Taylor, R. *J. Chem. Soc. Perkin Trans.* **1978**, *2*, 1255–1258.
[12] Scheer, J.C.; Kooyman, E.C.; Sixma, F.L. *Recl. Trav. Chim. Pays-Bas.* **1963**, *82* (7), 1123–1154.
[13] El-Gogary, T.M.; Heikal, L.A.; Abdel-Rahman, M.A.; El-Nahas, A.M. *Theor. Chem. Acc.* **2021**, *140* (3), 110.
[14] Kumgeh, B.A.; Bergthorson, J.M. *Combust. Flame* **2011**, *158* (6), 1037–1048.
[15] Mourits, F.M.; Rummens, H.A.; Sixma, F.L. *Can J. Chem.* **1977**, *55* (20), 3007–3020.
[16] Yang, B.; Westbrook, C.K.; Cool, T.A.; Hansen, N.; Kohse, H.K. *Z. Phys. Chem.* **2011**, *225* (11), 1293.
[17] Tan, T.; Yang, X.; Ju, Y.; Carter, E.A. *Phys. Chem. Chem. Phys.* **2015**, *17* (41), 31061–31072.
[18] Metcalfe, W.K.; Dooley, S.; Curran, H.J.; Simmie, J.M.; El-Nahas, A.M.; Navarro, M.V. *J. Phys. Chem. A* **2007**, *111* (13), 4001–4014.
[19] Ferrari, C.; Roche, A.; Jacob, V.; Foster, P.; Baussand, P. *Int. J. Chem. Kinet.* **1996**, *28*, 609–614.
[20] Atkinson, R. *J. Phys. Chem. Ref. Data Monograph* **1989,** *1*, 1–246.
[21] Kerr, J.A.; Stocker, D.W. *J. Atmos. Chem.* **1986**, *4*, 253–262.
[22] El Dib, G.; Mano Priya, A.; Lakshmipathi, S. *Atmosphere. (Basel)* **2022**, *13* (8), 1247.
[23] Kerr, J.A.; Stocker, D.W. *J. Atm. Chem.* **1986**, *4*, 263–276.
[24] Le Calvé, S.; Le Bras, G.; Mellouki, A. *Int. J. Chem. Kinet.* **1977**, *29*, 683–688.
[25] Picquet, B.; Heroux, S.; Chebbi, A.; Doussin, J.-F.; Durand-Jolibios, R.; Monod, A.; Loirat, H.; Carlier, P. *Int. J. Chem. Kinet.* **1998,** *30*, 839–847.
[26] Abdel-Rahman, M.A.; Shiroudi, A.; Kaya, S.; El-Nahas, A.M. *J. Mol. Struct.* **2022,** *1262*, 133006.
[27] Abdel-Rahman, M.A.; Shibl, M.F.; El-Demerdash, S.H.; El-Nahas, A.M. *Chemosphere* **2020,** *255*, 127031.
[28] Maeda, K.; Wall, M.L.; Carr, L.D. *New J. Phys.* **2015,** *17* (4), 045014.
[29] Zhao, Y.; Truhlar, D.G. *Theor. Chem. Acc.* **2008**, *120*, 215–241.
[30] Merrick, J.P.; Moran, D.; Radom, L. *J. Phys. Chem. A* **2007**, *111* (48), 11683–11700.
[31] Truhlar, D.G.; Kuppermann, A. *J. Am. Chem. Soc.* **1971,** *93* (7), 1840–1851.
[32] Gonzalez, C.; Schlegel, H.B. *J. Chem. Phys.* **1989,** *90* (5), 2154–2161.
[33] Gonzalez, C.; Schlegel, H.B. *J. Chem. Phys.* **1990,** *94* (7), 5523–5527.
[34] Wood, G.P.; Radom, L.; Petersson, G.A.; Barnes, E.C.; Frisch, M.J.; Montgomery, J.A. *J. Chem. Phys.* **2006,** *125* (9), 094106.

[35] Pople, J.A.; Head-Gordon, M.; Raghavachari, K. *J. Chem. Phys.* **1987,** *87*, 5968–5975.
[36] Sánchez-Márquez, J.; Zorrilla, D.; Sánchez-Coronilla, A.; de los Santos, D.M.; Navas, J.; Fernández-Lorenzo, C.; Alcántara, R.; Martín-Calleja, J. *J. Mol. Model.* **2014,** *20* (9), 2492.
[37] Parr, R.G.; Pearson, R.G. *J. Am. Chem. Soc.* **1983**, *105* (19), 7512–7516.
[38] Benchouk, W.; Mekelleche, S.M. *J. Mol. Struct.: Theochem.* **2008,** *852* (1-3), 46–53.
[39] Yang, W.; Parr, R.G. *Proc. Natl. Acad. Sci. U.S.A* **1985**, *82* (20), 6723–6726.
[40] Fuentealba, P.; Pérez, P.; Contreras, R. *J. Chem. Phys.* **2000,** *113* (6), 2544–2551.
[41] Mendizabal, F.; Donoso, D.; Burgos, D. *Chem. Phys. Lett.* **2011**, *514* (5-6), 374–378.
[42] Pérez, P.; Contreras, R. *Chem. Phys. Lett.* **1998,** *293* (3-4), 239–244.
[43] Burgos, D.; Olea-Azar, C.; Mendizabal, F. *J. Mol. Model.* **2012**, *18* (4), 2021–2029.
[44] Domingo, L.R.; Pérez, P.; Contreras, R. *Tetrahedron* **2004,** *60* (23), 6585–6591.
[45] Jensen, F. *Introduction to Computational Chemistry*, 2nd ed.; John Wiley & Sons: New Jersey, 2007, 133.
[46] Glowacki, D.R.; Wang, L.; Pilling, M.J. *J. Phys. Chem. A* **2009**, *113*, 5385–5396.
[47] Frisch, M.J.; Trucks, G.W.; Schlegel, H.B.; Scuseria, G.E.; Robb, M.A., Cheeseman, J.R., et al. *Gaussian 09*; Gaussian, Inc.: Wallingford, CT, 2013.
[48] Zhurko, G.A. *Chemcraft Program v.1.6*, 2014. https://www.chemcraftprog.com.
[49] Singleton, D.L.; Cvetanovic, R.J. *J. Am. Chem. Soc.* **1976,** *98*, 6812–6819.
[50] Canneaux, S.; Bohr, F.; Henon, E. *J. Comput. Chem.* **2014,** *35*, 82–93.
[51] Eyring, H. *J. Chem. Phys.* **1935**, *3*, 107–115.
[52] Eckart, C. *Phys. Rev.* **1930**, *35*, 1303–1309.
[53] Shiroudi, A.; Abdel-Rahman, M.A.; El-Nahas, A.M.; Altarawneh, M. *New J. Chem.* **2021**, *45*, 2237–2248.
[54] Nayebzadeh, M.; Vahedpour, M.; Shiroudi, A.; Rius-Bartra, J.M. *Chem. Phys.* **2019,** *528*, 110522.
[55] Uc, V.H.; Alvarez-Idaboy, J.R.; Galano, A.; Vivier-Bunge, A. *J. Phys. Chem. A* **2008**, *112*, 7608–7615.
[56] Abdel-Rahman, M.A.; Shibl, M.F.; El-Demerdash, S.H.; El-Nahas, A.M. *Comput. Theor. Chem.* **2019,** *1170*, 112634.
[57] Abdel-Rahman, M.A.; Shibl, M.F.; El-Nahas, A.M.; Abdel-Azeim, S.; El-Demerdash, S.H.; Al-Hashimi, N. *New J. Chem.* **2021**, *45*, 5907–5924.
[58] Zhou, C.-W.; Mebel, A.M.; Li, X.-Y. *J. Phys. Chem. A* **2009**, *113*, 10667–10677.
[59] Long, B.; Bao, J.L.; Truhlar, D.G. *Phys. Chem. Chem. Phys.* **2017**, *19*, 8091–8100.
[60] Long, B.; Bao, J.L.; Truhlar, D.G. *J. Am. Chem. Soc.* **2019**, *141*, 611–617.
[61] Herzberg, G. *Molecular Spectra and Molecular Structure. I. Spectra of Diatomic Molecules*; Van Nostrand: Princeton, NJ, 1950, pp. 194-204.
[62] Li, W.; Li, J.; Ning, H.; Shang, Y.; Luo, S.-N. *J. Phys. Chem. A* **2021**, *125*, 5103–5116.
[63] Lily, M.; Sutradhar, D.; Chandra, A.K. *Comput. Theor. Chem.* **2013**, *1022*, 50–58.
[64] Li, J.; Guo, H. *J. Phys. Chem. A* **2018**, *122*, 2645–2652.
[65] Gruber, B.; Czakó, G. *Phys. Chem. Chem. Phys.* **2020**, *22*, 14560-14569.
[66] Hammond, G.S. *J. Am. Chem. Soc.* **1955,** *77*, 334–338.
[67] Oller, J.; Pérez, P.; Ayers, P.W.; Vöhringer-Martinez, E. *Int. J. Quantum Chem.* **2018**, *118* (20), e25706.